Editors' Suggestion | Featured in Physics

Environment-Imposed Selection Rules for Nuclear-Spin Conversion of H_2 in Molecular Crystals

Nathan McLane*
Institute for Physical Science and Technology, University of Maryland, College Park, Maryland 20742, USA

LeAnh Duckett and Leah G. Dodson†
Department of Chemistry and Biochemistry, University of Maryland, College Park, Maryland 20742, USA

(Received 22 October 2025; accepted 20 February 2026; published 29 April 2026)

Nuclear-spin conversion in molecular hydrogen is governed by strict symmetry rules that typically require magnetic fields or catalytic surfaces to break. Here we demonstrate that the intrinsic tensor composition of a nonmagnetic molecular crystal field can impose and relax these rules without external fields. High-resolution infrared spectra of H_2 in crystalline CO_2 reveal large rank-2 (quadrupolar) crystal-field splittings of the m sublevels, while nuclear-spin conversion occurs only through $\Delta m = 0$ channels. Replacing CO_2 with polar N_2O introduces rank-1 (dipole) components that partially open $\Delta m \neq 0$ pathways, while incorporation of paramagnetic NO_2 fully lifts the restriction. These results establish a direct correspondence between crystal-field tensor rank and nuclear-spin dynamics, introducing a general symmetry-based framework for designing and controlling spin-isomer populations and quantum-state connectivity in molecular solids.

DOI: 10.1103/2yw9-7h62

The preparation and control of quantum states are central challenges in modern physics with implications ranging from quantum computing to energy storage [1–3]. The governing feature of quantum-state selection is the system symmetry, making symmetry one of the most powerful conceptual tools in molecular and condensed-matter physics [4–6]. The reduction of complex phenomena in many-body physics to group theoretical elements of the system allows a simplified interpretation of the system, and using methods such as the Wigner-Eckart theorem allows analysis of the selection rules and corresponding quantum dynamics of interacting matter [7]. These selection rules can apply to specific spectroscopic transitions, govern how the states of a system evolve, or define which channels are closed. The simplest neutral molecular example of state dynamic restriction based on symmetry properties is molecular hydrogen (H_2). H_2 is comprised of two nuclei containing fermionic protons that allow the molecule to be populated into two distinctive nuclear-spin states, *ortho*-H_2 and *para*-H_2. Given the symmetry requirements of the total wave function, there is no coupling of *ortho* and *para* states, consequently often resulting in nonequilibrium distributions of a given state [8]. To break the symmetry inherent in this system, anisotropic mechanisms have to be built in to induce conversion: paramagnet doping, surface interactions, and matrix confinement all suitably relax symmetry restrictions [9–15]. When H_2 is confined in a crystalline environment, the coupling between its spin states depends critically on the symmetries of both the guest (H_2) and the host lattice, leading to a range of exotic dynamical behaviors.

Previous studies have revealed rich symmetry-driven phenomena in confined hydrogen systems. For example, H_2 encapsulated in C_{60} exhibits strong translation-rotation coupling, while H_2 embedded in the C_2 phase of ice shows a pronounced splitting of the $j = 1$ *ortho* state [16–19]. These works primarily focused on the static properties of confined H_2; however, direct observation of time-dependent nuclear-spin conversion (NSC) dynamics has remained a challenge. In particular, experiments with C_{60} could not access these dynamics due to weak overlap between the nuclear-spin states, and similar temporal studies have yet to be carried out for the C_2 hydrogen-ice systems that exhibited such large splittings.

In this Letter, we demonstrate an environment-imposed selection rule for nuclear-spin conversion in nonmagnetic hosts through experiments and theoretical verification of H_2 confined in crystalline lattices [Fig. 1(a)]. The crystal field produced by diamagnetic CO_2 contains primarily rank-0 and rank-2 tensor components that result in large splitting of the *ortho*-H_2 magnetic sublevels; these states are spectroscopically distinguishable in infrared absorption measurements. The lattice has limited rank-1 content, prohibiting nuclear-spin conversion for $|\Delta m| = 1$, while coupling *ortho* and *para* states with $\Delta m = 0$ through the field's rank 0/2 elements. These observations are verified

*Contact author: nmclane@umd.edu
†Contact author: ldodson@umd.edu

 © 2026 American Physical Society

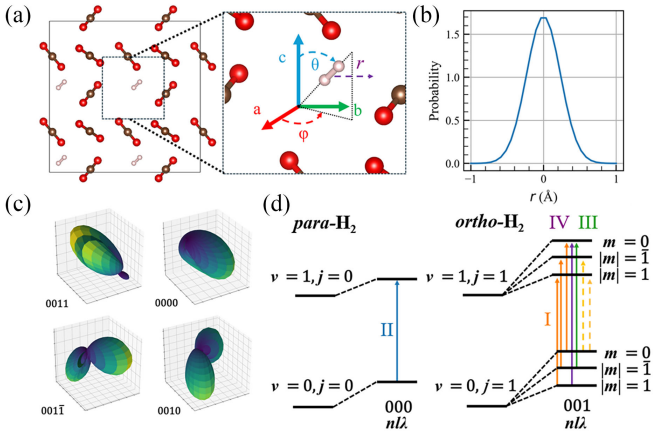


FIG. 1. (a) H_2 trapped in crystalline CO_2 experiences coupling between translational (as a function of r) and rotational (as a function of θ, ϕ) energies. (b) The four lowest-energy translational eigenfunctions have identical probability densities stemming from the harmonic potential. (c) Reduced probability density plots of the angular wave functions of the four lowest-energy states (shown with state designations $nl\lambda m$). (d) Solid arrows indicate rovibrational spectroscopic transitions that are allowed in the perturbed state, labeled with Roman numerals. Dashed arrows are suppressed transitions.

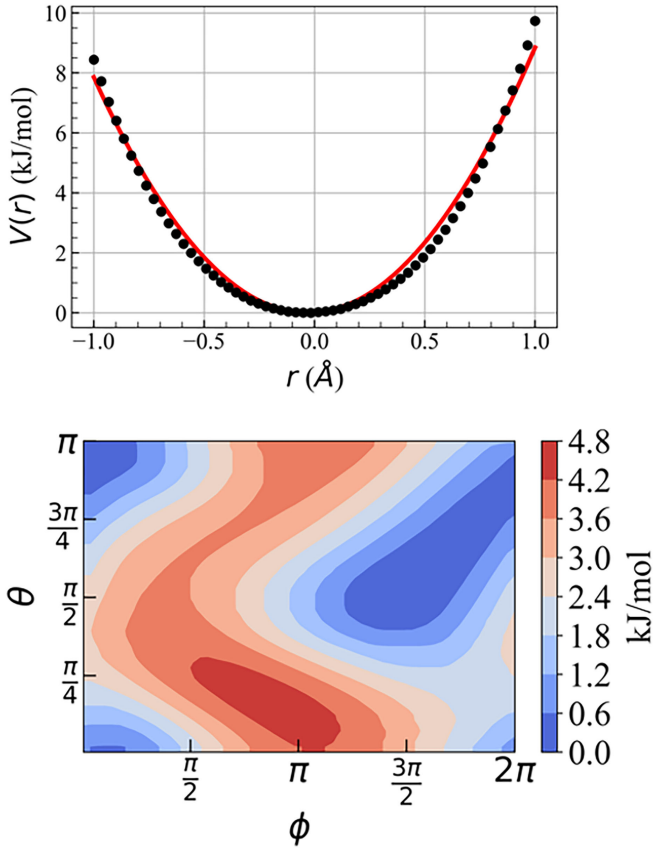


FIG. 2. Top: radial potential $V(r)$ for H_2 confined in CO_2 as a function of the translational distance r from equilibrium. The black dots are the calculated points, and the red line is a fit assuming a harmonic potential. Bottom: angular potential $V(\theta, \phi)$ for H_2 in CO_2 with respect to the two rotational degrees of freedom, θ and ϕ.

using control studies of crystalline N_2O and by adding a paramagnetic impurity NO_2.

The rotational-vibrational structure of H_2 is well described based on its fundamental vibrational frequency at 4161 cm^{-1} and rotational eigenenergies dictated by the rigid rotator with rotational constant $2B \approx 120$ cm^{-1} [20–22]. In confinement, the Hamiltonian acquires additional potential-energy terms that depend on the orientation (θ, ϕ) of the hydrogen molecule within its local environment and its translational motion (as a function of r) [16–19,23–26]. While confinement does perturb the vibrational motion, the vibrational energies are so much larger than the rotational and translational energy scales that no appreciable rotational-vibrational or translational-vibrational coupling occurs. Consequently, the translational-rotational states are effectively independent of vibrational state identity [16]. These perturbations can be expressed as a sum of spherical-tensor operators $T_q^{(k)}$ that represent the rank-k components of the surrounding crystal field [9]. Coupling between translational and rotational states results in a total angular momentum quantum number $\Lambda = L + J$ and corresponding eigenstates labeled by λ [16,17,27]. The anisotropic components of the crystal field lift the degeneracy of λ, splitting the energies of the magnetic sublevels m (the projections of Λ along the quantization axis) for *ortho*-H_2 [19]. In addition to splitting the m sublevels, the anisotropic components predicate the NSC process, causing decoherence in the angular momentum states that interconvert. The dominating component is the orientational potential on the H_2 molecule, while the translational potential has a negligible effect on NSC [17,28].

We assumed the effect of the crystalline lattice perturbs the rigid-rotor Hamiltonian through the addition of a potential term

$$V(r, \theta, \phi) = V(r) + V(\theta, \phi) + V(r)V(\theta, \phi), \quad (1)$$

where $V(r)$ is the isotropic translational confinement of H_2 and $V(\theta, \phi)$ is the angular potential of the local crystal field acting on the rotor. The coupling term $V(r)V(\theta, \phi)$ mixes translational and rotational motion due to similar energy scales, introducing cross terms between translational and rotational states and enabling small splittings [16–18,24,25,29,30]. The coordinates r, θ, ϕ, are defined according to Fig. 1(a), where r is the translation along the b axis, θ is the rotation about the a axis, and ϕ is the rotation about the c axis, which is the principal C_3 axis.

For simplicity we considered a primitive CO_2 unit cell, based on crystallographic information for the pure system [31], with a single H_2 molecule occupying a substitutional site. The potential functions $V(r)$ and $V(\theta, \phi)$ were computed using the CP2K package on the relaxed geometry obtained for the ground state at the PBE0 level

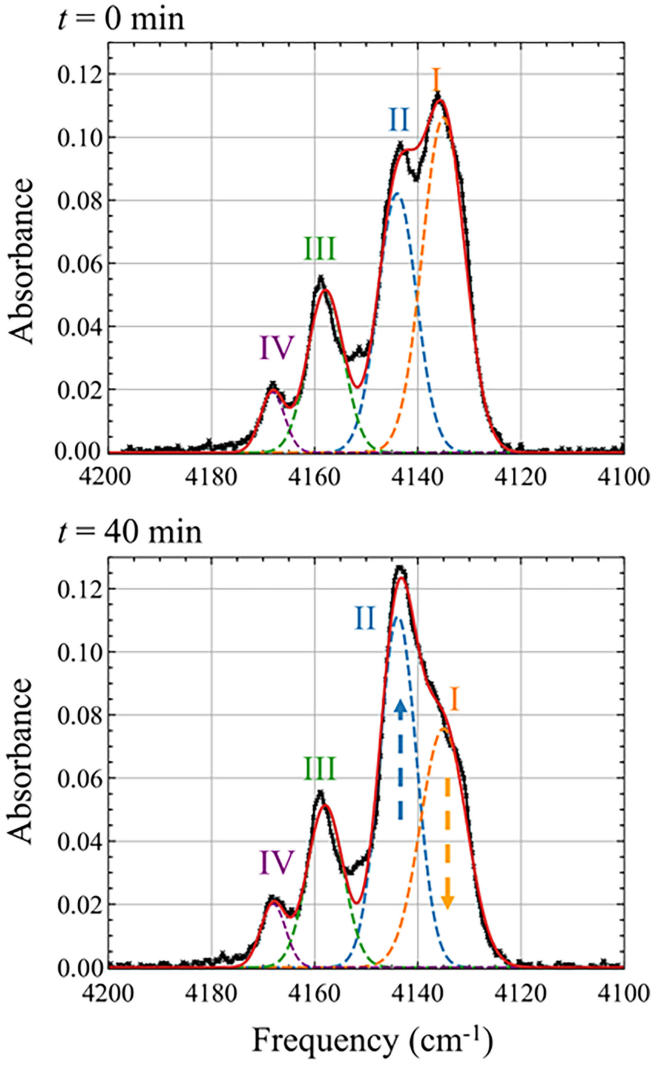


FIG. 3. The Q_1 spectral region of 1% H_2 confined in CO_2 at 10 K. Top: $t = 0$. Bottom: $t = 40$ min. Experimental data are shown in black. The dashed lines correspond to the individual fitted Gaussian peaks, and the red line is the linear combination of all fitted peaks.

(including an empirical dispersion correction) and TVZ2P basis with a plane wave cutoff of 600 Ry [32,33]. The translational potential $V(r)$ in Fig. 2 (top) is harmonic, whereas the angular potential $V(\theta, \phi)$ in Fig. 2 (bottom) exhibits significant anisotropy in the two-dimensional surface. Analytical fits to these potentials were then used to numerically obtain energies and wave functions [Figs. 1(b) and 1(c)] of the perturbed states (see Supplemental Material for further details [34]).

Deduction of specific j states are prescribed in Supplemental Material Sec. S1B [34], and eigenenergies for $j =$ even (*para*-H_2) and $j =$ odd (*ortho*-H_2) are diagrammed in Fig. 1(d), showing the splitting of the $|\lambda m\rangle$ states for $\lambda = 1$. The four lowest-energy perturbed states are reported in Supplemental Material Table S1 [34] and are destabilized with respect to the free-rotor states.

TABLE I. Summary of observed rovibrational transitions of H_2 in CO_2 or N_2O (cm^{-1}) identified by $|\lambda m\rangle \rightarrow |\lambda' m'\rangle$ during excitation from vibrational state $v = 0$ to $v' = 1$.

Peak	Transition	H_2 in CO_2	H_2 in N_2O
I	$\|1m\rangle \rightarrow \|1m\rangle$[a]	4134.4	4132.6[c]
II	$\|00\rangle \rightarrow \|00\rangle$	4143.9	4143.6
III	$\|1\bar{1}\rangle \rightarrow \|10\rangle$[b]	4158.1	4132.6[c]
IV	$\|11\rangle \rightarrow \|10\rangle$[b]	4168.2	4150.9

[a]For $m = 0, 1, \bar{1}$, with $\Delta m = 0$.
[b]$|\Delta m| = 1$.
[c]Assumed to be unresolved.

Higher-energy states and their tentative assignments to respective nuclear-spin states are also reported in Table S2 and Fig. S3 in Supplemental Material [34]. The m quantum numbers for *ortho*-H_2 are identified by inspection of the reduced probability density plots with respect to the z axis aligned to the C_3 symmetry axis of the CO_2 local environment. Because the local crystal field breaks azimuthal symmetry, the two $|m| = 1$ states are nondegenerate and are labeled arbitrarily $m = 1$ and $\bar{1}$. While there remains only a single rovibrational transition in the *para*-H_2 manifold, $\Delta m = 0$ and $|\Delta m| = 1$ transitions are possible during vibrational excitation of *ortho*-H_2 in the Q-branch manifold [20,21,40,41]. Solid lines in Fig. 1(d) indicate all expected transitions, whereas dashed lines indicate transitions that are symmetry suppressed, as seen previously [40]. Four observable spectroscopic transitions are therefore predicted: one transition for molecules in the *para* nuclear-spin state; and three nondegenerate transitions for molecules with $j = 1$: one threefold degenerate transition for $\Delta m = 0$ (orange arrows) and two transitions corresponding to $|\Delta m| = 1$ (green and purple arrows).

The rovibrational experimental spectrum of normal hydrogen trapped in crystalline carbon dioxide (1% H_2 in CO_2 at 10 K) confirms the prediction of four optical transitions, with four distinct peaks appearing in the Q_1 spectrum, as shown in Fig. 3. Peak centers, obtained from Gaussian fits to the experimental spectrum, are listed in Table I. The transition energies match those predicted by calculations. The lowest-energy peak (peak I, orange dashed line) corresponds to *ortho*-H_2 transitions from all three initial m states while obeying the strict $\Delta m = 0$ spectroscopic selection rule. The second-lowest-energy peak (peak II, blue dashed line) is the only peak corresponding to excitation of *para*-H_2 molecules, appearing 9.5 cm^{-1} higher in energy than the $\Delta m = 0$ *ortho* peak (predicted 16.8 cm^{-1}). The final two peaks (peaks III and IV, green and purple dashed lines) correspond to transitions of *ortho*-H_2 molecules starting in the $|m| = 1$ state prior to vibrational excitation and converting to $m' = 0$ in the vibrational excited state ($|\Delta m| = 1$). These two peaks are observed 23.7 and 33.8 cm^{-1} above the $\Delta m = 0$

peaks—qualitatively in line with prediction—and are weak as expected [40].

The time evolution of the experimental spectrum provides additional verification for assignments of these transitions: the intensity of peak I decreases from $t = 0$ to 40 min, whereas the intensity of peak II increases with time, implying a population transfer between the corresponding states. Significant intensity remains in peak I even after 40 min and does not decrease further. Surprisingly peaks III and IV do not change with time, even though they are assigned to metastable *ortho*-H_2. We expect initially deposited *ortho*-H_2 (room temperature *ortho*-to-*para* ratio $= 3:1$) to be driven by thermodynamics to convert to *para*-H_2 through external couplings that mediate nuclear-spin conversion. But in the nonmagnetic host, only the lowest-rank ($k = 0, 2$) components of the crystal-field tensor are appreciable, restricting the allowed nuclear-spin conversions to $\Delta m = 0$. Therefore, the loss of intensity in peak I confirms that some of its intensity originates from *ortho* molecules whose $m = 0$ sublevel can couple to *para*-H_2 via these even-rank tensor terms, and conversely the increase in peak II corroborates its assignment as belonging to the *para* manifold.

The persistence of peak I along with the time invariance of peaks III and IV demonstrates the absence of rank-1 tensor content in the host and confirms the resulting host-conditioned nuclear-spin-conversion selection rule. These three spectroscopic transitions (peaks I, III, IV) are assigned to rovibrational excitation of molecules in the *ortho* nuclear-spin state. At 10 K, the expected equilibrium *ortho*-to-*para* ratio is approximately 10^{-7}; thus, if nuclear-spin conversion channels were available, all H_2 molecules would relax to the *para* state. While nuclear-spin conversion is formally forbidden in the gas phase, this process can occur in nonmagnetic solids—particularly in quadrupolar CO_2—through even-rank rotational-spin, spin-lattice, and spin-spin dipolar interactions [11,14,15,42]. *ortho*-H_2 molecules initially in the $|10\rangle$ state can convert to *para*-H_2 ($|00\rangle$) through $\Delta j = -1$, $\Delta m = 0$ transitions driven by rank-0 and rank-2 perturbations of the crystal field. The observed population transfer between peak I (*ortho*-H_2) and II (*para*-H_2) corroborates this framework. The higher-energy peaks III and IV, assigned to molecules initially in the $|11\rangle$ and $|1\bar{1}\rangle$ states, require both $\Delta j = -1$ and $|\Delta m| = 1$; their invariance with time confirms that these channels remain closed in the absence of rank-1 contributions. The $|11\rangle$ and $|1\bar{1}\rangle$ substates also contribute to the lowest-energy rovibrational transition (peak I), and the nonzero asymptotic behavior of this peak further corroborates the closure of these channels.

Comparison with other host systems highlights how the confined environment dictates the perturbative nature and defines spectroscopic selection rules, the magnitude of the m energy splitting, and the channels available for nuclear-spin conversion. Amorphous CO_2 films lack the crystalline field needed to produce rank-2 tensor elements that clearly split m substates, while fast nuclear-spin conversion may occur through $|\Delta m| = 1$ mixing [12]. In endohedral C_{60} the local crystalline lattice, although sharing the same space group as CO_2, is nearly isotropic with very small distortions that contribute rank-2 content to create small splittings in the sublevels. Based on measured lifetimes, H_2 entrapped in C_{60} is assumed to have no open channels to nuclear-spin conversion [16–18,27,43,44]. In metal-organic frameworks [21,26,40,45], the metal sites will contribute rank-2 content, while absent rank-1 contributions, similarly leading to relatively large splittings in sublevel energies but without the large crystal-field gradients present in crystalline CO_2 that enable nuclear-spin conversion. Crystalline water ice (C_2 phase) is a host with large rank $0/1/2$ contributions, leading to large energy splittings and fast nuclear-spin conversion [13,19]. In the present Letter, complementary experiments replace CO_2 with its isoelectronic analog N_2O, which also forms the $Pa\bar{3}$ space group in low-temperature crystals [46]. N_2O will have reduced rank-2 content compared with CO_2 due to its smaller quadrupole, and the weak dipole moment adds an element of rank-1 coupling. We obtained $V(r)$ and $V(\theta, \phi)$ for crystalline N_2O (see Supplemental Material Sec. S3 for further details [34]) and used them to obtain the eigenfunctions and eigenenergies for this confined H_2 system and compared the expected optical transitions with spectra obtained for 1% H_2 in N_2O at 10 K (Fig. 4). The m-state energy splittings are still large (Table S1 in Supplemental Material [34]), but not as large as those of CO_2, verifying the importance of the dominant rank-2 tensor elements in CO_2. The degeneracy of the N_2O system is only partially lifted, with the two lowest-energy substates of *ortho*-H_2 remaining nearly degenerate. Transitions from these substates are observed as one single peak (peak N_2O-I/III) listed in Table I. The presence of a paramagnetic species like NO_2 introduces rank-1 tensor elements—at only 3% NO_2 impurity in a 1% H_2 in CO_2 at 10 K, all of the peaks assigned to *ortho*-H_2 disappear as the $|\Delta m| = 1$ channels open, and we are left with the *para*-H_2 peak; peak II in Fig. S4 in Supplemental Material [34]. The N_2O and NO_2 control experiments combine with the results of the present Letter to create a complete picture of the impact of the crystal field in molecular crystal lattices on the quantum dynamics of H_2.

While site effects are uncommon for low-concentration matrix-isolated diatomic molecules [47], the possibility that peaks III and IV may be caused by H_2 molecules trapped in geometrically distinct sites (e.g., interstitial sites of the crystalline CO_2) is tested using concentration-dependent studies. Increasing the guest-to-host ratio should increase the probability of guest molecules occupying energetically disfavored sites, leading to a corresponding increase in the observed absorption intensity of these sites. However, experiments conducted with 10% H_2 in CO_2 reveal the

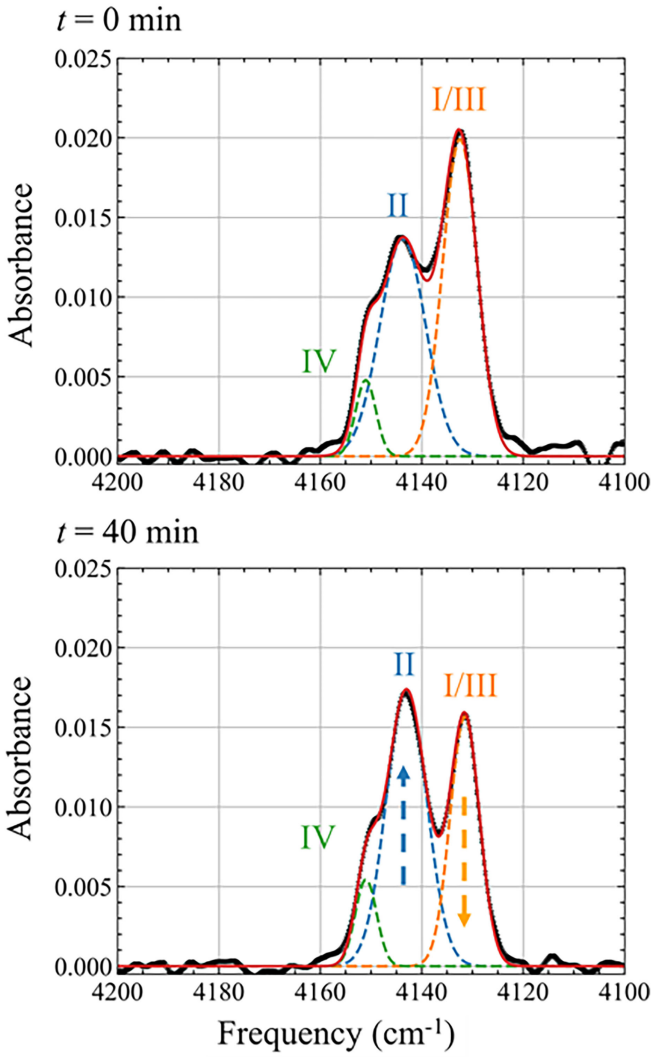


FIG. 4. The Q_1 spectral region of 1% H_2 in N_2O at 10 K. Top: $t = 0$. Bottom: $t = 40$ min. Experimental data are shown in black. The dashed lines correspond to the individual fitted Gaussian peaks, and the red line is the linear combination of all fitted peaks.

opposite trend, with peak IV disappearing entirely (Fig. S5 in Supplemental Material [34]). This is evidence to the contrary: that the H_2-H_2 interactions begin to increase at higher concentrations, causing, notably, an induced dipole canceling mechanism termed the "cancellation effect" [41,48] but no increase or introduction of new absorption features. These spectra also imply preferential binding of *ortho*-H_2 during the preliminary deposition process, which is revealed through the initial absence of peak II (*para*-H_2) immediately upon deposition. This preferential binding has been observed in other ices and van der Waals complexes [49,50]. The peak II intensity is ultimately recovered as *ortho*-H_2 $|10\rangle$ species in peak I convert to the *para* form.

In summary, crystalline CO_2 acts as a quantum-state filter that enforces a host-conditioned selection rule for nuclear-spin conversion of H_2. The nonmagnetic lattice provides strong rank-2 (quadrupolar) anisotropy but negligible rank-1 (vector) content, yielding large splittings of the m sublevels yet restricting nuclear-spin conversion to the $\Delta m = 0$ channel. Replacing CO_2 with polar N_2O introduces weak rank-1 components that partially relax this restriction, while paramagnetic NO_2 fully opens all spin-conversion channels. Together these results establish a direct correspondence between the tensor composition of the local field and the available nuclear-spin pathways. Although a complete microscopic mechanism for nuclear-spin conversion in solids remains an open question, our measurements place clear constraints on the underlying couplings. The selective observation of $\Delta m = 0$ conversion in CO_2 is consistent with nonmagnetic, even-rank interactions such as spin-rotation and spin-lattice couplings, whereas the activation of $\Delta m \neq 0$ channels in N_2O and NO_2 demonstrates the role of local dipolar or paramagnetic fields. These results show that lattice symmetry dictates which couplings can contribute, providing a symmetry-based framework for future mechanistic studies.

Beyond hydrogen, this "tensor-engineered" control of state connectivity offers a design principle for manipulating quantum-state populations in simple molecular solids. By revealing that lattice symmetry alone defines the allowed spin-conversion channels, this Letter extends familiar selection-rule concepts from atomic, molecular, and optical physics into condensed-phase molecular solids. Such direct and coherent interconversion between pure spin states opens new possibilities for realizing molecular qubits, probing local field anisotropies, and symmetry-based control of quantum-state evolution in condensed environments.

Acknowledgments—This material is based upon work supported by the U.S. Department of Energy, Office of Science Early Career Research Program, Office of Basic Energy Sciences under Award No. DE-SC0024262. The authors acknowledge the University of Maryland supercomputing resources [51] made available for conducting the research reported in this Letter.

Data availability—The data that support the findings of this article are openly available [52].

[1] A. Gaita-Ariño, F. Luis, S. Hill, and E. Coronado, Nat. Chem. **11**, 301 (2019).
[2] M. R. Wasielewski, M. D. E. Forbes, N. L. Frank, K. Kowalski, G. D. Scholes, J. Yuen-Zhou, M. A. Baldo, D. E. Freedman, R. H. Goldsmith, T. Goodson, M. L. Kirk, J. K. McCusker, J. P. Ogilvie, D. A. Shultz, S. Stoll, and K. B. Whaley, Nat. Rev. Chem. **4**, 490 (2020).
[3] Y. Zhou, W. Yuan, M. Li, Z. Xie, X. Song, Y. Yang, J. Wang, L. Li, W. Ding, W.-F. Lin, and Z. Wei, Nat. Energy **9**, 1297 (2024).

[4] S. D. Ivanov, O. Asvany, A. Witt, E. Hugo, G. Mathias, B. Redlich, D. Marx, and S. Schlemmer, Nat. Chem. **2**, 298 (2010).
[5] J. Yu and C.-X. Liu, Nat. Commun. **11**, 2290 (2020).
[6] P. Zhu, Z. Liu, X. Lei, S. He, D. Wang, J. Zeng, L. Wang, F. Su, W. Peng, Z. Liang, Y. Sun, Z. Lei, Z. Li, H.-Y. Hsu, X. Pan, X. Wang, J. Li, Y. Zhang, and B. Xu, Nat. Synthesis **5**, 64 (2025).
[7] E. Wigner, *Gruppentheorie und ihre Anwendung auf die Quantenmechanik der Atomspektren* (Vieweg+Teubner Verlag, Wiesbaden, 1931), 10.1007/978-3-663-02555-9.
[8] G. Herzberg, *Molecular Spectra and Molecular Structure. I. Spectra of Diatomic Molecules* (D. Van Nostrand Company, Inc, Princeton, NJ, 1950).
[9] S. E. Nielsen and J. S. Dahler, J. Chem. Phys. **46**, 732 (1967).
[10] E. Ilisca and F. Ghiglieno, Eur. Phys. J. B **87**, 235 (2014).
[11] P. A. Fedders, Phys. Rev. B **20**, 2588 (1979).
[12] K. Yamakawa, A. Ishibashi, T. Namiyoshi, Y. Azuma, and I. Arakawa, Phys. Rev. B **102**, 041401(R) (2020).
[13] L. Senadheera and M. S. Conradi, J. Phys. Chem. A **112**, 8303 (2008).
[14] P. A. Fedders, Phys. Rev. B **63**, 165201 (2001).
[15] P. A. Fedders, Phys. Rev. B **34**, 7489 (1986).
[16] S. Mamone, J. Y.-C. Chen, R. Bhattacharyya, M. H. Levitt, R. G. Lawler, A. J. Horsewill, T. Rõõm, Z. Bačić, and N. J. Turro, Coord. Chem. Rev. **255**, 938 (2011).
[17] S. Mamone, M. Ge, D. Hüvonen, U. Nagel, A. Danquigny, F. Cuda, M. C. Grossel, Y. Murata, K. Komatsu, M. H. Levitt, T. Rõõm, and M. Carravetta, J. Chem. Phys. **130**, 081103 (2009).
[18] T. Yildirim and A. B. Harris, Phys. Rev. B **66**, 214301 (2002).
[19] S. Di Cataldo, M. Rescigno, L. Monacelli, U. Ranieri, R. Gaal, S. Klotz, J. Ollivier, M. M. Koza, C. De Michele, and L. E. Bove, Phys. Rev. Lett. **133**, 236101 (2024).
[20] S. A. FitzGerald, J. Hopkins, B. Burkholder, M. Friedman, and J. L. C. Rowsell, Phys. Rev. B **81**, 104305 (2010).
[21] S. A. FitzGerald, K. Allen, P. Landerman, J. Hopkins, J. Matters, R. Myers, and J. L. C. Rowsell, Phys. Rev. B **77**, 224301 (2008).
[22] B. P. Stoicheff, Can. J. Phys. **35**, 730 (1957).
[23] L. Pauling, Phys. Rev. **36**, 430 (1930).
[24] T. Yildirim and A. B. Harris, Phys. Rev. B **67**, 245413 (2003).
[25] R. J. Cross, J. Phys. Chem. A **105**, 6943 (2001).
[26] I. Matanović, J. L. Belof, B. Space, K. Sillar, J. Sauer, J. Eckert, and Z. Bačić, J. Chem. Phys. **137**, 014701 (2012).
[27] S. Ye, M. Xu, S. FitzGerald, K. Tchernyshyov, and Z. Bačić, J. Chem. Phys. **138**, 244707 (2013).
[28] Y. Miyamoto, M. Fushitani, D. Ando, and T. Momose, J. Chem. Phys. **128**, 114502 (2008).
[29] R. M. Herman and J. C. Lewis, Phys. Rev. B **73**, 155408 (2006).
[30] F. Sebastianelli, M. Xu, Y. S. Elmatad, J. W. Moskowitz, and Z. Bačić, J. Phys. Chem. C **111**, 2497 (2007).
[31] S. Gražulis, A. Daškevič, A. Merkys, D. Chateigner, L. Lutterotti, M. Quirós, N. R. Serebryanaya, P. Moeck, R. T. Downs, and A. Le Bail, Nucleic Acids Res. **40**, D420 (2012).
[32] T. D. Kühne *et al.*, J. Chem. Phys. **152**, 194103 (2020).
[33] C. Adamo and V. Barone, J. Chem. Phys. **110**, 6158 (1999).
[34] See Supplemental Material at http://link.aps.org/supplemental/10.1103/2yw9-7h62 for details of the theoretical model and experimental methods, which include Refs. [35–39], results from control experiments, and a list of all eigenenergies computed for this work.
[35] E. K. Hockey, K. Vlahos, T. Howard, J. Palko, and L. G. Dodson, J. Phys. Chem. A **126**, 3110 (2022).
[36] E. K. Hockey, N. McLane, K. Vlahos, L. M. McCaslin, and L. G. Dodson, J. Chem. Phys. **160**, 094303 (2024).
[37] R. M. Escribano, G. M. Muñoz Caro, G. A. Cruz-Diaz, Y. Rodríguez-Lazcano, and B. Maté, Proc. Natl. Acad. Sci. U.S.A. **110**, 12899 (2013).
[38] K. Isokoski, C. A. Poteet, and H. Linnartz, Astron. Astrophys. **555**, A85 (2013).
[39] S. Grimme, J. Antony, S. Ehrlich, and H. Krieg, J. Chem. Phys. **132**, 154104 (2010).
[40] L. Kong, Y. J. Chabal, and D. C. Langreth, Phys. Rev. B **83**, 121402 (2011).
[41] J. Van Kranendonk and H. Gush, Phys. Lett. **1**, 22 (1962).
[42] G. Pileio, Prog. Nucl. Magn. Reson. Spectrosc. **56**, 217 (2010).
[43] M. Xu, F. Sebastianelli, B. R. Gibbons, Z. Bačić, R. Lawler, and N. J. Turro, J. Chem. Phys. **130**, 224306 (2009).
[44] Y. Kohama, T. Rachi, J. Jing, Z. Li, J. Tang, R. Kumashiro, S. Izumisawa, H. Kawaji, T. Atake, H. Sawa, Y. Murata, K. Komatsu, and K. Tanigaki, Phys. Rev. Lett. **103**, 073001 (2009).
[45] S. A. FitzGerald, C. T. Eckdahl, C. S. McDonald, J. N. Nelson, K. Shinbrough, H. W. H. Lai, and J. L. C. Rowsell, Phys. Rev. B **92**, 134304 (2015).
[46] A. A. Solodovnik, Low Temp. Phys. **35**, 339 (2009).
[47] L. Andrews and M. Moskovits, *Chemistry and Physics of Matrix-Isolated Species* (North-Holland, Amsterdam, Oxford, New York, 1989).
[48] H. P. Gush, E. J. Allin, H. L. Welsh, and W. F. J. Hare, Can. J. Phys. **38**, 176 (1960).
[49] T. A. Grinev, A. A. Buchachenko, and R. V. Krems, Chem. Phys. Chem. **8**, 815 (2007).
[50] V. Buch and J. P. Devlin, J. Chem. Phys. **98**, 4195 (1993).
[51] http://hpcc.umd.edu.
[52] The data that support the findings of this study are available in Figshare at 10.6084/m9.figshare.30385903.